Materials Advances

ROYAL SOCIETY OF CHEMISTRY

PAPER

View Article Online
View Journal

Cite this: DOI: 10.1039/d5ma00709g

Bimetallic melamine doped ZnCo-ZIF-8 derived carbons as bifunctional ORR/OER electrocatalysts for zinc–air batteries

Lingfei Kong and Volkan Degirmenci *

Zinc–air batteries are promising for energy storage due to their high energy density, low-cost and safety, yet their performance is limited by sluggish oxygen reduction reaction (ORR) and oxygen evolution reaction (OER) kinetics. Developing efficient bifunctional catalysts is thus crucial for advancing metal–air batteries. In this study, a porous carbon nanomaterial embedded with cobalt nanoparticles is synthesized through the pyrolysis of a Co–Zn bimetallic zeolitic imidazolate framework (ZIF) doped with melamine, demonstrating exceptional activity as a bifunctional ORR & OER catalyst. The catalyst yields a nitrogen-doped porous carbon with carbon nanotube structure. The further optimisation of the synthesis conditions revealed a catalyst (mCo_3Zn_1@CN(800)) showing significant bifunctional electrocatalytic activity for ORR and OER, giving a low potential gap (ΔE) of 0.68 V, which matches the precious metals based benchmark materials. The catalyst shows excellent activity in ORR with onset potential of 0.98 V and half-wave potential of 0.89 V with a Tafel slope of 44.6 mV dec^{-1}. Similarly, it shows remarkable OER activity with overpotential (η_{OER}) of 0.34 V at 10 mA cm^{-2}. Furthermore, a series of these catalysts were employed as air electrode in a Zn–air battery, achieving a high open-circuit voltage of 1.430 V, and exhibiting excellent cycling stability over 250 hours (1250 cycles) at 2 mA cm^{-2}. The enhanced electrochemical performance could be attributed to the characteristics of the catalysts, including high surface area with well dispersed, exposed, and stable Co–N_x active sites, as well as graphitic carbon and carbon nanotubes. These features collectively promote the oxygen reactions of both OER and ORR.

Received 4th July 2025,
Accepted 19th August 2025

DOI: 10.1039/d5ma00709g

rsc.li/materials-advances

1. Introduction

The growing demand for sustainable and high-performance energy storage technologies has drawn significant attention to metal–air batteries due to their low cost, environmental friendliness, and high energy density.[1] Among these, zinc–air batteries (ZABs) are particularly promising, benefiting from the abundance and safety of zinc.[2,3] However, the commercialisation of ZABs remains hindered by the sluggish kinetics of the oxygen reduction reaction (ORR) during discharge and the oxygen evolution reaction (OER) during recharge.[4] Therefore, developing efficient and stable bifunctional electrocatalysts for ORR and OER is a critical challenge.[5]

Transition metal oxides, while widely explored, often suffer from issues such as nanoparticle aggregation, low conductivity, and limited surface area.[6] To overcome these limitations, metal–organic frameworks (MOFs), particularly zeolitic imidazolate frameworks (ZIFs), have been investigated as precursors for electrocatalyst synthesis.[7,8] Upon pyrolysis, MOFs can be converted into conductive carbon structures embedded with metal or metal oxide nanoparticles, yielding materials with high porosity and active site density.[9–13]

MOF-derived carbon electrocatalysts have shown considerable promise for oxygen electrocatalysis. For instance, Fe–Co/N-doped carbons derived from ZIFs have demonstrated excellent performance,[14–16] owing to their hierarchical porosity, strong metal–nitrogen coordination, and structural stability.[17,18] Nitrogen doping plays a key role in stabilising non-noble metal active sites, forming M–N_x configurations known to enhance ORR/OER activity.[19–22] In particular, ZIF-8 and ZIF-67 have served as common platforms due to their high surface areas and thermal stability.[23] During pyrolysis, the formation of M–N_x–C sites is promoted by the presence of metal–nitrogen bonds in the framework and can be further enhanced using nitrogen-rich precursors such as melamine.[23–27] In recent years, studies[28–30] have focused on the development of ZIF-derived M–N–C catalysts with tuneable compositions and porous frameworks to enhance ORR/OER bifunctionality in ZABs. Particularly, Co-based systems with hierarchical structures and heteroatom doping have shown promising electrochemical performance, due to their optimized active site exposure and mass transfer properties.

University of Warwick, School of Engineering, CV4 7AL, UK.
E-mail: v.degirmenci@warwick.ac.uk

Despite extensive efforts, it remains challenging to achieve materials that simultaneously exhibit hierarchical porosity, high graphitisation, uniform heteroatom distribution, and direct carbon nanotube (CNT) formation—features that collectively enhance bifunctional electrocatalytic performance.

In this study, we address these challenges by synthesizing a nitrogen-doped graphitic carbon material embedded with Co nanoparticles and CNTs, derived from a melamine-modified Co–Zn bimetallic ZIF-8 precursor. Melamine not only enhances nitrogen doping and CNT formation but also suppresses particle aggregation during pyrolysis. The combination of Co-ZIF-8 with melamine and controlled Co/Zn ratios enables the formation of a porous, conductive carbon matrix with optimally exposed Co–N_x sites. The resulting catalyst exhibits outstanding bifunctional activity for both ORR and OER in alkaline conditions, outperforming commercial Pt/C and RuO_2 benchmarks. Our findings demonstrate a practical route toward scalable, MOF-derived bifunctional catalysts for next-generation zinc–air batteries.

2. Experimental

2.1. Chemicals

All materials were purchased and used as available: zinc nitrate hexahydrate ($Zn(NO_3)_2{\cdot}6H_2O$, >99%, Thermo Fisher), 2-methylimidazole (MeIm, 99%, Aldrich), copper nitrate hexahydrate ($Co(NO_3)_2{\cdot}6H_2O$, >99%, Aldrich), methanol (CH_3OH, >99.9%, Aldrich), melamine (99%, Thermo Fisher), potassium hydroxide (KOH, flake, >85%, Thermo Fisher), Nafion (6% PFSA in lower aliphatic alcohols and water, Aldrich), carbon-supported platinum (20% on carbon black powder, Thermo Fisher), carbon black (Super P Conductive, 99 + %, metal basis, Thermo Fisher), poly(vinylidene fluoride) ($(-CH_2CF_2-)_n$, 99%, Thermo Fisher) and DI water (12.5 MΩ cm).

2.2. Synthesis

2.2.1. Synthesis of Co-ZIF-8. The synthesis of Co-ZIF-8 was conducted following a literature-reported procedure with modifications.[31] Initially, cobalt nitrate hexahydrate $Co(NO_3)_2{\cdot}6H_2O$ (0.8730 g, 1 mmol) and zinc nitrate hexahydrate $Zn(NO_3)_2{\cdot}6H_2O$ (0.2975 g, 0.333 mmol) in varying (*x*/*y*, *e.g.* 3/1) molar ratios were dissolved in 80 mL of methanol to form a homogenous solution. The solution was then poured into methanol (80 mL) solution containing 75 mmol 2-methylimidazole (6.1575 g) with vigorous stirring for 24 hours at room temperature. The product was separated and collected by centrifuge, followed by washing with methanol three times. The washed product was then dried in a vacuum oven at 70 °C for 24 hours. Materials were synthesized with varying molar ratios of Co to Zn.

2.2.2. Synthesis of mCo-ZIF-8. A mixture of melamine (400 mg) and Co-ZIF-8 (200 mg) was dissolved in 100 mL of methanol with vigorous stirring for 10 hours. The resulting product was then separated by centrifuge and dried overnight in a vacuum oven at 70 °C. It is labelled as mCo-ZIF-8, where initial m represents the melamine addition.

2.2.3. Synthesis of carbons mCo_xZn_y@CN(T). mCo-ZIF-8 was evenly dispersed in a ceramic boat, and directly pyrolyzed at varying temperatures (700 °C, 800 °C, 850 °C) for 3 hours in a tubular furnace under an Argon atmosphere, with a heating rate of 5 °C min^{-1}. After cooling to room temperature, the resulting product was collected without further treatment. It is labelled as: mCo_xZn_y@CN(T) where initial m represents the melamine addition, subscripts *x*, *y* represents the molar ratios of Co to Zn, and T represents pyrolysis temperature. As a comparison, a batch of carbon materials were prepared directly from Co-ZIF-8 without melamine doping and labelled as Co_xZn_y@CN(T).

2.3. Characterization

The physical and chemical properties of catalysts were analysed by various techniques. The crystalline structure of the carbon materials was determined by X-ray diffraction (XRD) experiments, employing a Panalytical X'Pert Pro MPD (Malvern Panalytical, Malvern, United Kingdom) equipped with monochromatic Cu $K_{\alpha 1}$ radiation and a PIXcel solid-state detector. Thermal stability of the catalysts was investigated using a thermogravimetric analysis (TGA) instrument (Mettler Toledo, Columbus, Ohio, OH, USA) under nitrogen and air flow (50 mL min^{-1}) at ambient pressure, heating samples from 25 °C to the desired temperature, typically 900 °C, at a rate of 10 °C min^{-1}. A Nicolet Nexus 470 Fourier transform infrared (FTIR) spectrometer (Thermo Fisher Scientific, Waltham, MA, USA.) was used to identify the functional groups in the samples. N_2 physisorption measurements were conducted at −196 °C using a Micromeritics ASAP2020, after degassing the samples at 200 °C for 4 h. Surface areas were calculated using the Brunauer–Emmett–Teller (BET) method. Elemental analysis was performed using a Varian 720 ES Inductively Coupled Plasma Optical Emission Spectroscopy (ICP-OES), calibrated with 5, 10 and 20 ppm standard solutions prepared from certified 1000 ppm reference solutions. Samples were digested using a microwave-assisted acid digestion method with a mixture of sulphuric and perchloric acids and analysed with a blank prepared at the same time. X-Ray fluorescence (XRF, Rigaku Primus IV) spectrometer was also used to determine the elemental composition at room temperature without prior treatment. Scanning electron micrographs and elemental maps were obtained by using a Zeiss SUPRA 55-VP scanning electron microscope with a large area silicon drift detector energy dispersive X-ray spectroscopy (SDD EDX) detector operating at 5 keV high-angle and double aberration-corrected JEOL ARM 200F, a high-resolution annular dark-field scanning transmission electron microscope (HAADF-STEM) with a windowless large solid angle EDX. The X-ray photoelectron spectroscopy (XPS) data were collected at the Warwick Photoemission Facility, University of Warwick. The samples were attached to electrically conductive carbon tape, mounted on to a sample bar and loaded into a Kratos Axis Ultra DLD spectrometer which possesses a base pressure below 1×10^{-10} mbar. The measurements were conducted at room temperature. The data were analysed in the Casa XPS package and KherveFitting,[32] using Shirley

backgrounds and mixed Gaussian Lorentzian (Voigt) line shapes.

2.4. Electrochemical performance

The electrocatalytic activities for ORR and OER were evaluated using an electrochemical workstation (Metrohm Autolab PGSTAT 128N) in a standard three-electrode system. Pt foil and Ag/AgCl (3 M KCl) were used as the counter and reference electrodes, respectively. First, the glassy carbon electrode was polished with the slurry of alumina powder. Each catalyst (5 mg) was ultrasonically dispersed into a solution containing 750 μL of ethanol, 250 μL of water, and 20 μL of 5 wt% Nafion for 2 h. Subsequently, approximately 10 μL of the above homogenous catalyst ink was evenly dropped onto the freshly polished glassy carbon electrode (5 mm in diameter) with a loading of around 14 g cm^{-2} and dried naturally at room temperature. Then, the well-prepared glassy carbon electrode was used as the working electrode (cross section for current passing: 0.0707 cm^2). Another catalyst slurry was prepared by mixing 30 mg of catalyst, 200 mg of active carbon black, and 995 μL of PVDF (used as a polymer binder, prepared by dissolving 0.2 g of PVDF in 10 mL of NMP), followed by grinding in a mortar. A square stainless mesh with a diameter of 2 cm, coated with the slurry, used as the working electrode with a loading was around 10 g cm^{-2}. The ORR/OER electrochemical experiments were then carried out in O_2-saturated 1 M KOH electrolyte. All current densities were normalized to the cross-section area for current passing, and the measured potentials (*vs.* the Ag/AgCl reference) were converted to the reversible hydrogen electrode (RHE) scale based on the Nernst equation (eqn (1)).

$$E_{RHE} = E_{Ag/AgCl} + 0.059 \times pH + E^0_{Ag/AgCl}\,(0.197\ V) \quad (1)$$

Before each test, the electrolyte was bubbled with pure N_2 or O_2 for at least 30 minutes and maintained above the surface of the electrolyte during the measurements. Cyclic voltammetry (CV) experiments were conducted in both N_2-saturated and O_2-saturated 1 M KOH electrolyte at a scan rate of 50 mV s^{-1}. Linear sweep voltammetry (LSV) measurements were performed in the O_2-saturated 1 M KOH electrolyte at a scan rate of 10 mV s^{-1}. The commercial Pt/C (20%) and RuO_2 were fabricated as the benchmark electrodes for ORR and OER, respectively. Rotating disk electrode (RDE) experiments were carried out to evaluate the ORR reactions, with rotating rates varying from 1600 rpm to 100 rpm. Electrochemical impedance spectroscopy (EIS) was measured from 0.5 MHz to 0.1 Hz with a 10 mV AC voltage, and Nyquist curves were obtained for these electrocatalysts. EIS fitting results and corresponding equivalent circuit model are given in Table S1.

2.5. Rechargeable zinc–air battery tests

Long-term stability tests for zinc–air batteries were conducted *via* the Neware battery cycling testing system (CT-4008Tn-5V100mA-124). The zinc–air battery contains a Zn plate as the metal anode, catalysts as the air electrode, and a solution of 6 M KOH and 0.2 M $Zn(OAc)\cdot 2H_2O$ as the electrolyte. For the air electrode, a slurry of the electrode catalyst prepared with PVDF was deposited onto a 2 × 2 cm stainless mesh. Additionally, charge–discharge galvanostatic tests were conducted with each cycle lasting for 10 minutes, comprising 5 min of charging, and 5 min of discharging at a current density of 2 mA cm^{-2}.

3. Results

3.1 Properties of catalysts

Cobalt doped ZIF-8 catalysts were synthesized at room temperature by mixing cobalt and zinc precursors, followed by the addition of the organic linker, 2-methylimidazole, in methanol under vigorous stirring overnight. The crystalline structure of Co-ZIF-8 samples were observed by XRD, which confirms the successful formation of a typical ZIF-8 structure (Fig. 1(a)). The XRD patterns show characteristic peaks of ZIF-8, centred at lower 2θ values of 5, 11, 13 and the pattern is identical to a simulated reference spectrum. The XRD patterns of Melamine embedded materials (mCo-ZIF-8) show characteristic peaks of ZIF-8 and additional peaks originated from melamine at 2θ of 26.5° and a shoulder at 18° (Fig. 1(a), and Fig. S1). The sharp peaks observed in the XRD spectra indicate the high crystallinity of Co-ZIF-8 and mCo-ZIF-8 catalysts.

The FT-IR spectra of Co-ZIF-8 and mCo-ZIF-8 are shown in Fig. 1(b), revealing that both materials exhibit similar peaks, consistent with the literature.[33] The peaks around 690 cm^{-1} indicate the C–H band of 2-methylimidazole. The peak at 1145 cm^{-1} shows =C–H in-plane deformation vibration whereas at approximately 1308 cm^{-1} and 1423 cm^{-1}, the asymmetric band of $-CH_3$ and $-CH_2$ can be observed, respectively. The C=C double bond stretch is visible at 1460 cm^{-1}, while the C=N double bond stretching is visible at 1582 cm^{-1}. Two small peaks at around 2928 cm^{-1} and 3134 cm^{-1} confirm the C–H symmetric and =C–H stretch, respectively. Additionally, a series of the absorption bands at 3420 cm^{-1} and 3460 cm^{-1} indicate the stretching of $-NH_2$, characteristic of the melamine (see Fig. S2)[34] which confirms the successful addition of melamine in ZIF-8 structure.

Both Co-ZIF-8 and mCo-ZIF-8 samples were pyrolyzed at temperatures 700 °C, 800 °C, and 850 °C under Argon atmosphere. After pyrolysis a graphitised carbon has been formed. In Fig. 1(c) both Co_3Zn_1@CN(800) and mCo_3Zn_1@CN(800) show a broad XRD diffraction peak, centring at 25.0° and a shoulder at 43.7°, corresponding to the (002) and (101) reflections of graphitized carbon, respectively. Three distinct peaks are observed at 44.8°, 52.2°, and 76.5°, indicating Co (111), Co (200), and Co (220), respectively. The SEM EDX mapping of the mCo_3Zn_1@CN materials indicate that the elements are well distributed on the carbon framework (Fig. S3–S5).

The comparison of TGA curves of Co-ZIF-8 and mCo-ZIF-8 reveals a different decomposition pattern for each catalyst (Fig. 1(d)). Co-ZIF-8 remains stable up to 506 °C, whereas the less thermally stable mCo-ZIF-8 is firstly decomposed around 275 °C, with a sharp weight loss of 69.6%, indicating an

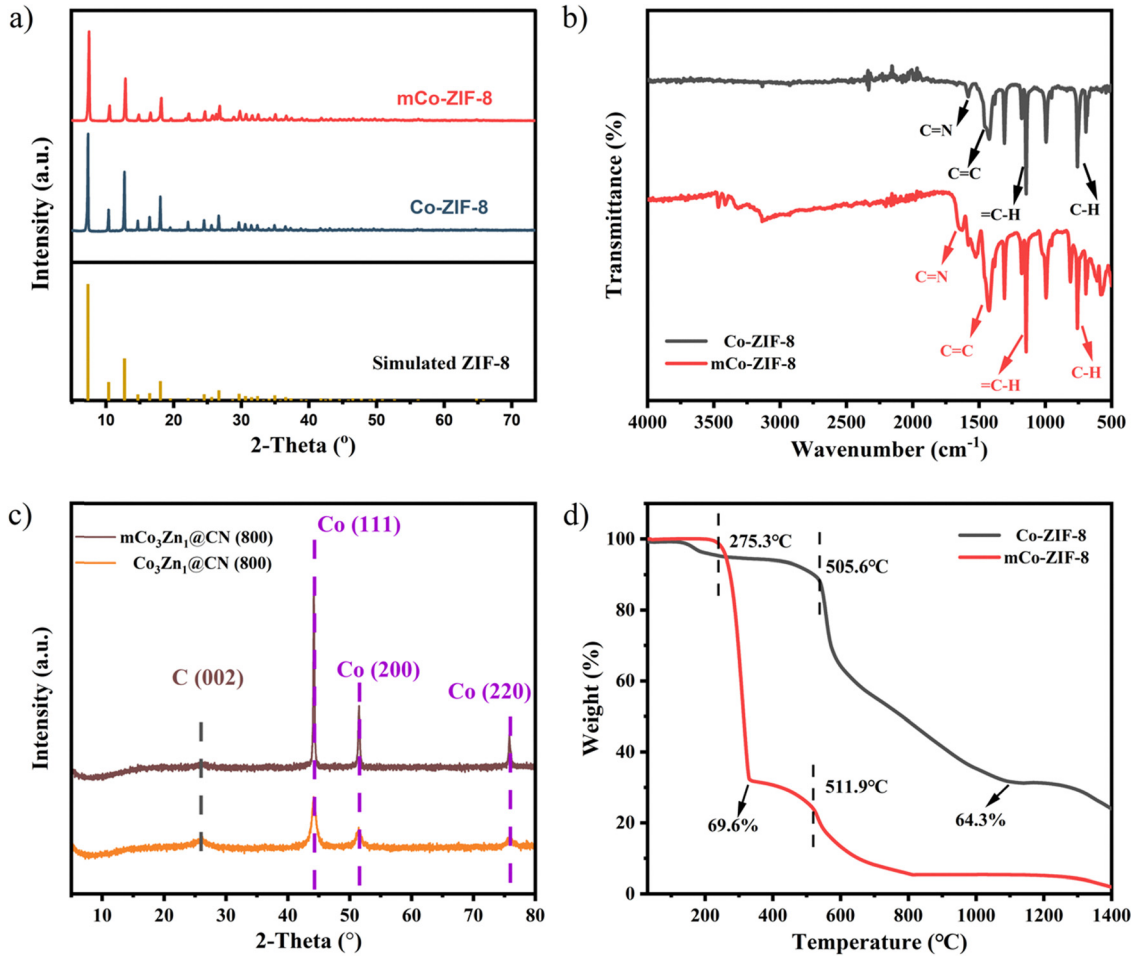

Fig. 1 (a) XRD patterns of simulated ZIF-8, Co-ZIF-8 and mCo-ZIF-8, (b) FTIR patterns of the Co-ZIF-8 and mCo-ZIF-8, (c) XRD patterns of Co_3Zn_1@CN(800) and mCo_3Zn_1@CN(800), (d) TGA curves of the Co-ZIF-8 and mCo-ZIF-8.

accelerated decomposition of the organic linkers. Therefore, in the pyrolysis, a plausible mechanism for carbonization process unfolds as follows: (a) imidazole linkers tend to transform into N-doped porous carbon, and zinc species evaporate; (b) during the pyrolysis process, with the participation of melamine, corrosive gaseous species, *e.g.* NH_3, are released, attacking ligand–metal bonds and dissociating the ligands. This is supported by the fact that melamine doped catalyst (mCo-ZIF-8) was pyrolyzed completely and there is no weight loss after 810 °C. The elemental analysis of Co-ZIF-8 material revealed an expected Co to Zn molar ratio of around 0.3 (Table S1). On the other hand, after pyrolysis, the carbon materials show much higher Co/Zn ratios, indicating that the Zn is partially evaporated at high temperatures. These results (Table S1) confirm that only trace amounts of Zn remained after pyrolysis—0.09 wt% in the 850 °C sample and 0.44 wt% in the 800 °C sample. These low values suggest that most Zn was effectively removed by 850 °C. Later, we systematically evaluated the ORR and OER catalytic performance of mCo_xZn_y@CN(T) samples pyrolyzed at 700 °C, 800 °C, and 850 °C. The residual Zn may influence the catalytic properties of the final material. Our findings indicated that mCo_xZn_y@CN(800) exhibited superior catalytic activity compared to samples synthesized at other temperatures, thereby negating the necessity to explore pyrolysis temperatures beyond 850 °C. This suggests that the small amount of retained Zn may contribute positively through a synergistic effect, possibly by promoting porosity or affecting local coordination environments. Additionally, TEM analysis provided direct evidence that melamine doping significantly facilitated the formation of distinct nanotube structures specifically at 800 °C (Fig. S6), a phenomenon not observed at other investigated pyrolysis temperatures.

Samples pyrolyzed at 800 °C with varying Co/Zn molar ratios were further analysed using X-ray photoelectron spectroscopy (XPS) (Fig. 2 and Fig. S7–S9). The high-resolution XPS spectra for the C 1s, N 1s, and Co 2p regions of mCo_3Zn_1@CN(800) are presented in Fig. 2(a)–(c), respectively. The obtained spectra align well with previously reported data on similar materials.[35–39] The high-resolution C 1s spectrum can be deconvoluted into three distinct peaks corresponding to C–C (284.8 eV), C–N (285.6 eV), and O–C=O (288.3 eV), indicating successful doping of nitrogen into the carbon matrix. Deconvolution of the N 1s region (Fig. 2(b)) reveals four characteristic peaks at 398.4 eV (pyridinic-N), 399.2 eV (Co–N_x), 400.1 eV (pyrrolic-N), and

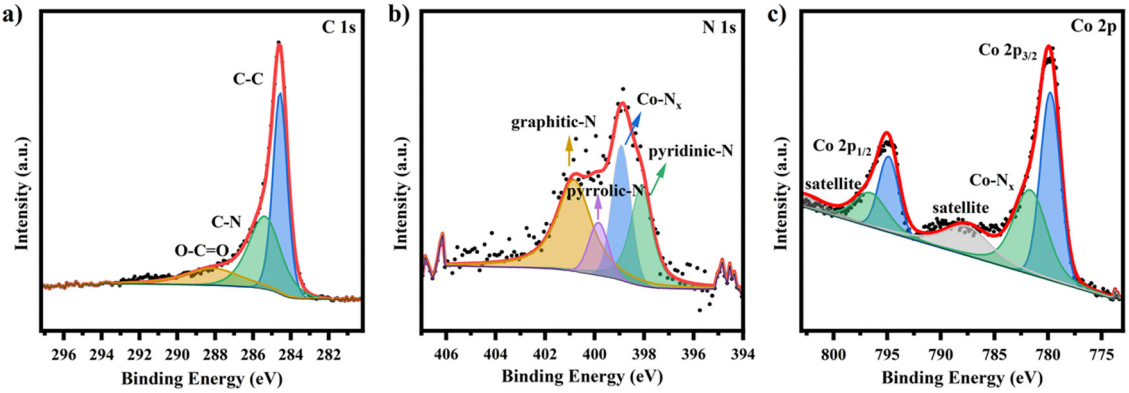

Fig. 2 High-resolution XPS spectra of mCo_3Zn_1@CN(800): (a) C 1s, (b) N 1s, (c) Co 2p.

401.1 eV (graphitic-N). Pyridinic-N and pyrrolic-N species introduce defects into the carbon framework, whereas graphitic-N contributes to enhanced electrical conductivity. The Co 2p spectrum (Fig. 2(c)) displays characteristic peaks at Co $2p_{3/2}$ and Co $2p_{1/2}$, associated with Co–O (780.1 eV and 795.1 eV) and Co–N_x (781.9 eV and 796.8 eV) interactions. Similarly, the XPS spectra of mCo_1Zn_3@CN(800) (Fig. S8) resemble those of mCo_3Zn_1@CN(800). However, an additional set of peaks at 778.4 eV and 793.2 eV is observed in the Co 2p spectrum of mCo_1Zn_1@CN(800) (Fig. S9), corresponding to metallic Co, indicating variations in the cobalt species due to the differing Co/Zn molar ratios. The mCo_1Zn_1@CN(800) sample exhibits a prominent Co–N_x peak, meanwhile the relative intensity of pyrrolic-N is lower compared to that of graphitic-N. Given that pyrrolic and pyridinic nitrogen species are introducing defects into the carbon matrix, which can contribute positively to catalytic activity, the lower concentration of these defect-related sites may partially account for the weaker ORR/OER performance of the mCo_1Zn_1@CN(800) material relative to the mCo_3Zn_1@CN(800) material. While Co–N_x moieties are recognized as primary active sites for ORR and OER, their presence alone does not fully account for the observed activity. Rather, the enhanced performance may arise from a more complex interplay involving defect density, the formation of carbon nanotube structures, and the synergistic integration of these features within the catalyst architecture.

The morphology of the materials was examined using TEM and SEM. As shown in Fig. 3, ZIF-8, Co-ZIF-8, and mCo-ZIF-8

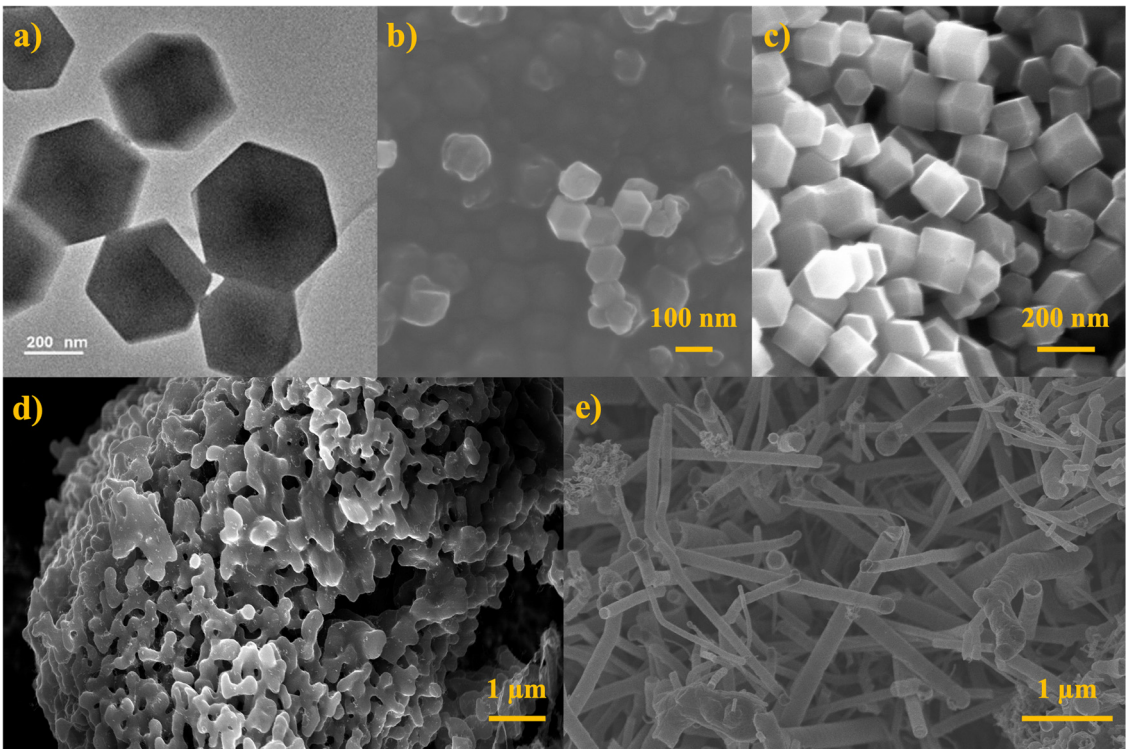

Fig. 3 TEM image of ZIF-8 (a) and SEM images of the catalysts: (b) Co-ZIF-8, (c) mCo-ZIF-8, (d) Co_3Zn_1@CN(800), (e) mCo_3Zn_1@CN(800).

exhibit a well-defined truncated rhombic dodecahedral morphology with uniform particle sizes, consistent with previous reports.[40,41] This indicates that the incorporation of cobalt and melamine does not alter the morphology of ZIF-8. Upon pyrolysis, the materials are converted into graphitized carbon. Notably, the melamine-doped mCo_3Zn_1@CN(800) sample exhibits distinct carbon nanotube (CNT) structures, which are absent in the undoped counterpart (Fig. 3(d) and (e)). These nanotube structures are particularly prominent in the sample pyrolyzed at 800 °C as compared to 700 °C and 850 °C (Fig. S10). Fig. S11 presents the effect of varying Co/Zn ratios at 800 °C and CNT features are observed across all Co/Zn molar ratios (1/1, 1/3, and 3/1), but appear more clearly in the 3/1 ratio. The formation of these nanotube structures is attributed to the high-temperature decomposition of melamine and the catalytic effect of the Co-ZIF-8 framework. Melamine, in particular, has been previously reported to facilitate CNT formation during pyrolysis.[42] In addition to morphological features, the mCo_3Zn_1@CN(800) sample exhibits a porous structure with a high specific surface area. Nitrogen adsorption–desorption isotherms reveal a Type IV hysteresis loop, characteristic of mesoporous materials, and the highest BET surface area among the series, measured at 1130.7 $m^2\ g^{-1}$ (Fig. S12 and Table S2). These results confirm that mCo_3Zn_1@CN(800) exhibits a highly porous carbon nanotube-rich structure, whereas mCo_3Zn_1@CN(850) shows signs of densification, structural collapse, and particle aggregation. This observation suggests that thermal decomposition-induced structural reconstruction plays a key role in shaping the final carbon morphology. Furthermore, SEM-EDX elemental mapping of the mCo_x-Zn_y@CN(800) series confirms the homogeneous distribution of Co, Zn, and N throughout the carbon matrix (Fig. S3–S5).

To further investigate the structure of the materials, we conducted high-angle annular dark-field scanning transmission electron microscope (HAADF-STEM) analysis. As seen in Fig. 4(a), Co-ZIF-8 possesses dodecahedron shape with the elements Co, Zn, C, and N dispersed evenly in the MOF framework. After the pyrolysis of the melamine doped material, at 700 °C, the Co phase prevailed, and the carbon turned out to be solely nanotube structure (Fig. 4(b)). Co atoms accumulated at the growth tips of carbon nanotubes. Pyrolysis at 800 °C results in better-formed nanotubes (Fig. 4(c)). On the other hand, a

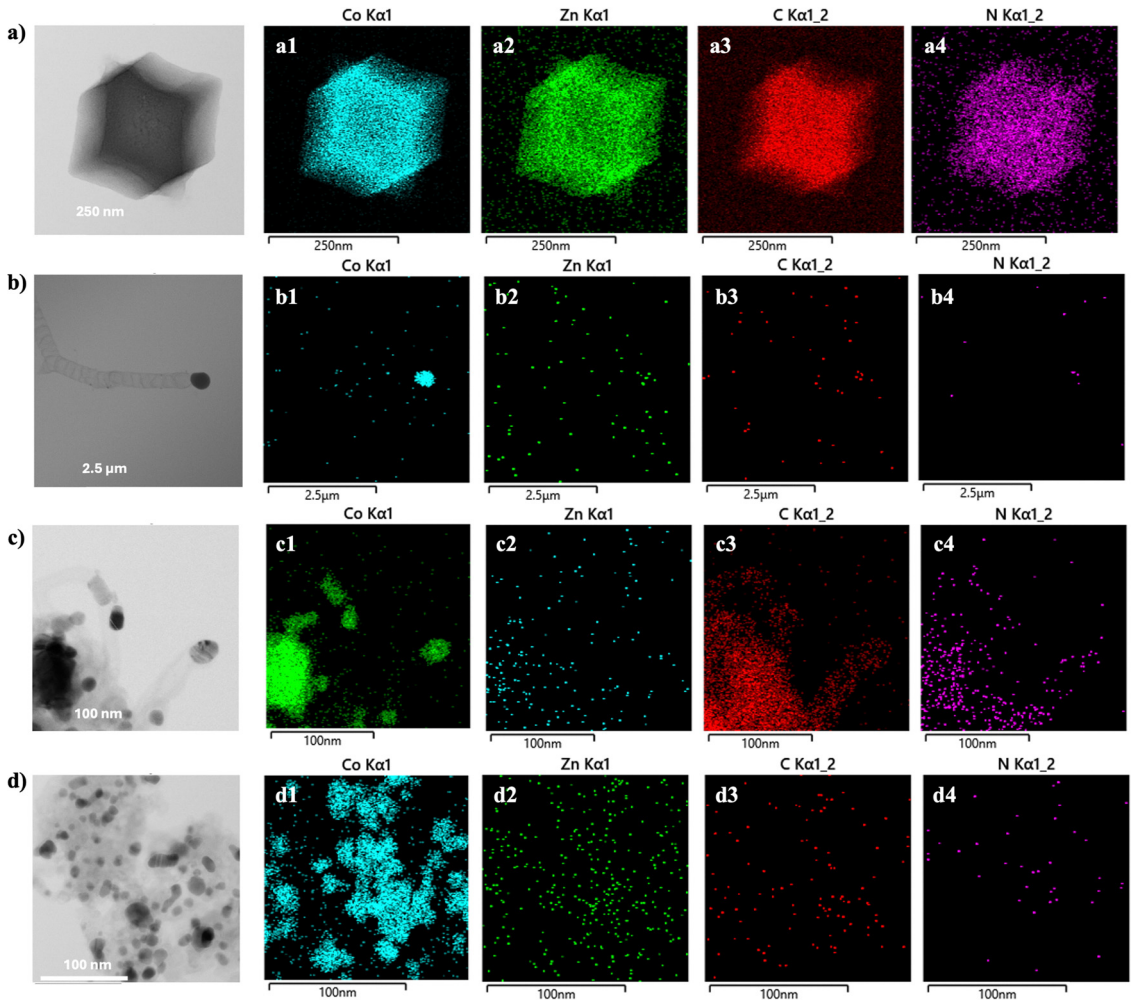

Fig. 4 HAADF-STEM images of the catalysts: (a) Co-ZIF-8, (b) mCo_3Zn_1@CN(700), (c) mCo_3Zn_1@CN(800), (d) mCo_3Zn_1@CN(850).

further increase in the pyrolysis temperature to 850 °C, leads to a material in which the Co atoms aggregate into large clusters, as seen in Fig. 4(d), (d1)–(d4). Therefore, 800 °C is chosen to be an optimum pyrolysis temperature.

3.2 ORR and OER electrocatalytic activities

Major electrochemical properties of the materials are listed in Table 1 in comparison to benchmark precious metal Ru and Pt based catalysts. Oxygen reduction peaks were observed under O_2-saturated conditions, as evidenced by cyclic voltammetry (CV) curves compared to N_2-saturated solutions (Fig. S13). Carbon materials derived from melamine-containing ZIF-8s exhibited significant electrocatalytic activity, whereas non-melamine-derived carbons showed considerably lower activity. The activities of catalysts in oxygen evolution reaction (OER) and oxygen reduction reaction (ORR) were further investigated through linear sweep voltammetry (LSV) measurements. Analysis of the OER LSV curve (Fig. 5(a)) reveals that mCo_3Zn_1@CN(800) has the smallest onset potential (0.12 V) among the other catalysts, only slightly larger than the benchmark RuO_2 (0.08 V) (Fig. S14). To deliver a 10.0 mA cm^{-2} current density, the required potential ($E_{j=10,\,OER}$) of mCo_3Zn_1@CN(800) is 1.57 V, while the required potential of RuO_2 is 1.51 V, and mCo_1Zn_1@CN(800) is 1.59 V. mCo_3Zn_1@CN(800) exhibits the smallest onset potential and required potential ($E_{j=10,\,OER}$). The theoretical OER onset potential is 1.23 V *vs.* RHE in both acidic and alkaline media and the OER overpotential (η_{OER}) is calculated as: $\eta_{OER} = E_{j=10,\,OER} - 1.23$ V. The mCo_3Zn_1@CN(800) gives the smallest overpotential (η_{OER}) of 0.34 V. Tafel slopes were extracted from LSV curves to evaluate the OER kinetics of the catalysts and shown in Fig. 5(b). For comparison, the Tafel slopes of OER follow the sequence: RuO_2 (83.6 mV dec^{-1}) < mCo_3Zn_1@CN(800) (123.9 mV dec^{-1}) < mCo_1Zn_3@CN(800) (130.3 mV dec^{-1}) < mCo_1Zn_1@CN(800) (130.9 mV dec^{-1}) < mCo_6Zn_1@CN(800) (146.9 mV dec^{-1}) < mCo_1Zn_1@CN(800) (148.8 mV dec^{-1}).

The ORR electrocatalytic activity was evaluated in O_2-saturated 1 M KOH solutions with rotating disk electrode (RDE) experiments (Fig. 5(c) and Fig. S15). Materials derived from melamine doped and non-doped Co-ZIF-8 with varying pyrolysis temperatures are compared in Fig. S15. The melamine-based materials, mCo_3Zn_1@CN(T)'s, exhibit smaller onset potentials, half-wave potentials, and the Tafel slopes as compared to their non-doped counterparts (Fig. S15). In particular, the mCo_3Zn_1@CN(800) exhibits the best ORR activity with the lowest diffusion-limited current density (j_L = 5.68 mA cm^{-2} at 1600 rpm), the largest onset potential ($E_{onset,\,ORR}$ = 0.98 V), and the largest half-wave potential ($E_{1/2}$ = 0.87 V). To analyse the ORR kinetics, the Koutecky–Levich (K–L) equation was applied. It is seen that the K–L plots show linear relationship (Fig. 5(d)) between the potentials of 0.1 V and 0.3 V, and materials have close slope values. The corresponding average electron transfer number (n) has a value of 3.65, indicating a preferred four-electron dominant ORR pathway.

Furthermore, the potential gap, ΔE ($\Delta E = E_{j=10,\,OER} - E_{1/2,\,ORR}$), was calculated for the catalysts. mCo_3Zn_1@CN(800) has the lowest potential gap (0.68 V) which indicates that mCo_3Zn_1@CN(800) catalyst is an efficient ORR & OER bifunctional catalyst. In general, the decrease in resistance could improve the performance of electrocatalysts, which could be resulted from the presence of pyridinic-N and carbon nanotubes.[43] The Nyquist curve plots conducted under OER conditions (Fig. 5(e)) shows mCo_3Zn_1@CN(800) has the smallest R_{CT} (charge transfer resistance) = 6.07 Ω among all catalysts where the simulated circuits are shown in Fig. 5(f). In comparison, among all the catalysts, mCo_3Zn_1@CN(800) gives accelerated kinetics for OER and ORR consistently.

With the Co/Zn ratio of 3/1 confirmed to exhibit the best electrocatalytic performance, we investigated the samples with Co/Zn ratio of 3/1 in more detail (Fig. 6). Fig. 6(a) shows the OER LSV curves of melamine doped and non-doped mCo_3Zn_1@CN(T) pyrolyzed at temperatures, 700, 800, and 850 °C. Among all the catalysts, mCo_3Zn_1@CN(800) showed the best OER performance with smallest onset potential (0.12 V). To deliver a 10.0 mA cm^{-2} current density, the required potential of mCo_3Zn_1@CN(800) is 1.570 V, and Co_3Zn_1@CN(800) is 1.683 V, slightly higher than RuO_2 (0.35 V) (Fig. S14). After doping melamine, the OER performance of all the catalysts were improved, closer to benchmark RuO_2. Other OER properties of the materials are listed in Table 1. Tafel slopes extracted from the OER LSV curves are shown in Fig. 6(b). mCo_3Zn_1@CN(800) shows the smallest Tafel slope

Table 1 OER and ORR electrochemical properties[a] of materials with and without melamine doping pyrolyzed at different temperatures and their comparison to benchmark precious metal RuO_2 and Pt/C catalysts

Catalyst	$E_{1/2}$ (V)	j_L (mA cm^{-2})	$E_{j=10,\,OER}$ (V)	η_{OER}	ΔE (V)	Tafel slope (mV dec^{-1})
mCo_3Zn_1@CN(700)	0.88	4.8	1.622	0.392	0.742	62.7
mCo_3Zn_1@CN(800)	0.89	5.3	1.570	0.340	0.680	44.6
mCo_3Zn_1@CN(850)	0.86	4.8	1.615	0.385	0.755	87.9
Co_3Zn_1@CN(700)	0.66	2.7	1.698	0.468	1.038	74.0
Co_3Zn_1@CN(800)	0.87	3.1	1.683	0.453	0.813	50.0
Co_3Zn_1@CN(850)	0.87	4.8	1.644	0.414	0.774	67.3
RuO_2	na	na	1.510	0.280	na	83.57
Pt/C	0.89	6.2	na	na	na	66.19

[a] $E_{1/2}$ represents for the half-wave potential of ORR, j_L stands for the diffusion-limited current density, $E_{j=10,\,OER}$ is the OER potential corresponding to a current density of 10 mA cm^{-2}. $\Delta E = E_{j=10,\,OER} - E_{1/2}$, is the potential gap a measure for the overall bifunctional ORR & OER activity. η_{OER} is the OER overpotential. The theoretical OER onset potential is 1.23 V *vs.* RHE in both acidic and alkaline media. The OER overpotential is calculated as: $\eta_{OER} = E_{j=10,\,OER} - 1.23$ V. na stands for not applicable.

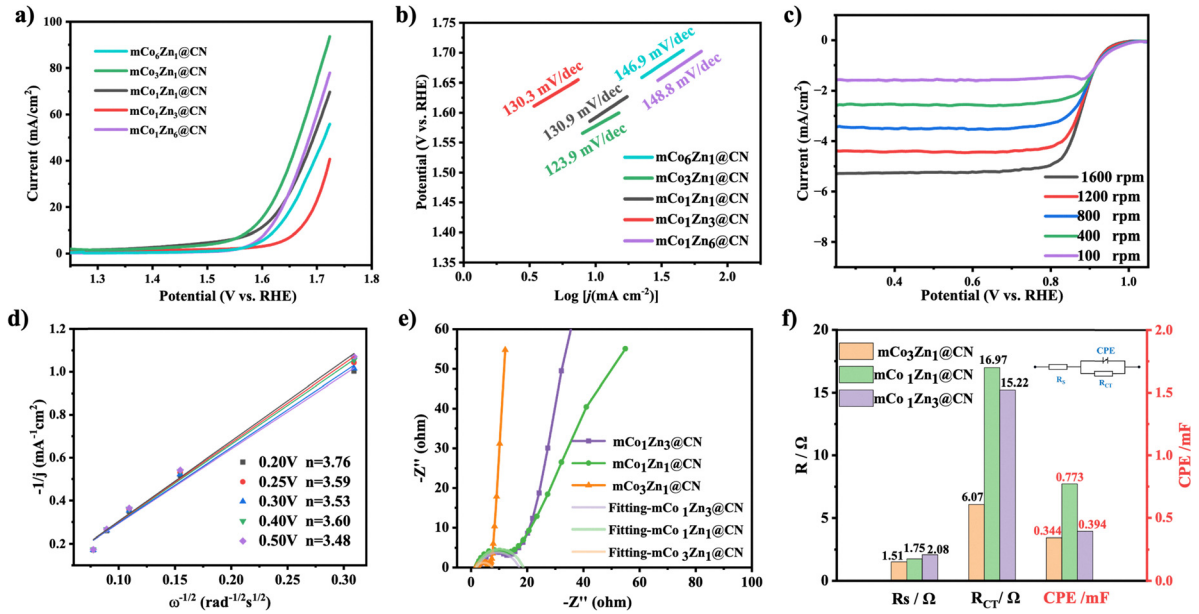

Fig. 5 (a) OER LSV plots of mCo_xZn_y@CN(800) catalysts with varying Co to Zn ratios, pyrolyzed at 800 °C. (b) Tafel slopes of OER obtained from OER LSV plots. (c) ORR LSV plots of mCo_3Zn_1@CN(800) (d) K–L plots of mCo_3Zn_1@CN(800) between potentials 0.05 V and 0.35 V obtained from ORR. (e) Fitting curves of Nyquist radius responses for R_{CT} (charge transfer resistance) obtained from OER. (f) Comparison of parameters for equivalent circuit fitting results obtained from OER.

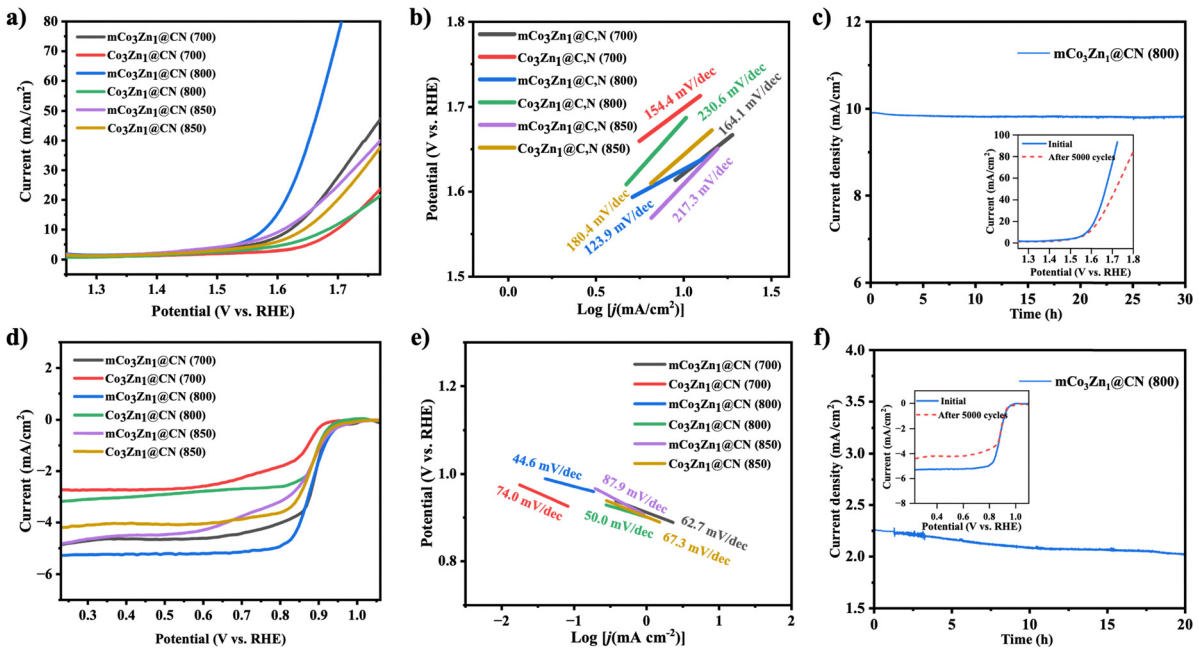

Fig. 6 LSV curves of Co_3Zn_1@CN(T) and mCo_3Zn_1@CN(T) with varying pyrolysis temperatures. Top line of graphs, (a)–(c) shows the OER results, whereas the bottom line of graphs (d)–(f) shows the ORR results. (a) OER LSV, (b) Tafel slope from OER LSV, (c) Chronopotentiometry curves for mCo_3Zn_1@CN(800) and inset graph OER LSV curves measured on mCo_3Zn_1@CN(8) before and after 5000 cycles, (d) ORR LSV, (e) Tafel slope from ORR LSV, (f) Chronopotentiometry curves for mCo_3Zn_1@CN(800) and inset graph ORR LSV curves measured on mCo_3Zn_1@CN(800) before and after 5000 cycles.

(109.1 mV dec^{-1}) than others (Fig. 6(b)), indicating the enhanced OER kinetics.

The ORR activity was tested by RDE between speeds of 1600 rpm to 100 rpm for each catalytic material pyrolyzed at different temperatures with the same Co/Zn ratio of 3/1 (Fig. S15). Meanwhile, Fig. 6(d) shows the comparison of ORR LSV curves of the same catalysts (Co_3Zn_1@CN(T) and mCo_3Zn_1@CN(T)) at 1600 rpm. As seen in Fig. 6(d) mCo_3Zn_1@CN(800) shows

the best ORR activity with the lowest diffusion-limited current density (j_L = 5.68 mA cm^{-2}), the best onset potential (E_{onset} = 0.98 V), the best half-wave potential ($E_{1/2}$ = 0.89 V), and the smallest Tafel slope of 44.6 mV dec^{-1}. In addition, it shows a very low charge transfer resistance (Table S3), $R_{CT} < 7\ \Omega$ indicates efficient electron transfer kinetics, help improving overall electrocatalytic performance. As compared to the benchmark Pt/C (j = 6.21 mA cm^{-2}, E_{onset} = 1.06 V, and $E_{1/2}$ = 0.89 V) (Fig. S16), mCo_3Zn_1@CN(800) is an effective ORR catalyst with superior performance. The chronopotentiometry curves for mCo_3Zn_1@CN(800) showed steady performance in both OER and ORR (Fig. 6(c) and (f), respectively) throughout the continuous electrocatalysis process without obvious fluctuations or drops in current density. Moreover, exceptional cyclic stability for OER and ORR are further evidenced by testing LSV before and after 5000 cycles CV runs (inset Fig. 6(c) and (f)).

3.3 Rechargeable Zn–air battery

The rechargeable ZABs were assembled using Zn plate as the metal anode, mCo_3Zn_1@CN(800) as the air electrode, and a solution of 6 M KOH and 0.2 M $Zn(OAc)_2{\cdot}2H_2O$ as the electrolyte. Fig. 7(a) and (b) represents the rechargeable ZAB in ORR reaction and OER reaction, respectively. As shown in Fig. 7(c), the open circuit voltage (OCV) of the battery is 1.430 V, matching the theoretical value of the Zn–air battery.[44,45] The charge/discharge polarization curve is shown in Fig. 7(d). The battery gives a current density of 74.8 mA cm^{-2} at 0.72 V, and the maximum power density reaches 102.9 mW cm^{-2} at 279 mA cm^{-2}. The discharge plot recorded at a current density of 2 mA cm^{-2} which is shown in Fig. 7(e). The voltage dropped sharply to 1.17 V at the beginning and then remains stable for 65 h without any further obvious voltage drop. Afterwards, the voltage dropped until the Zn plate was penetrated during the corrosion. The corresponding specific

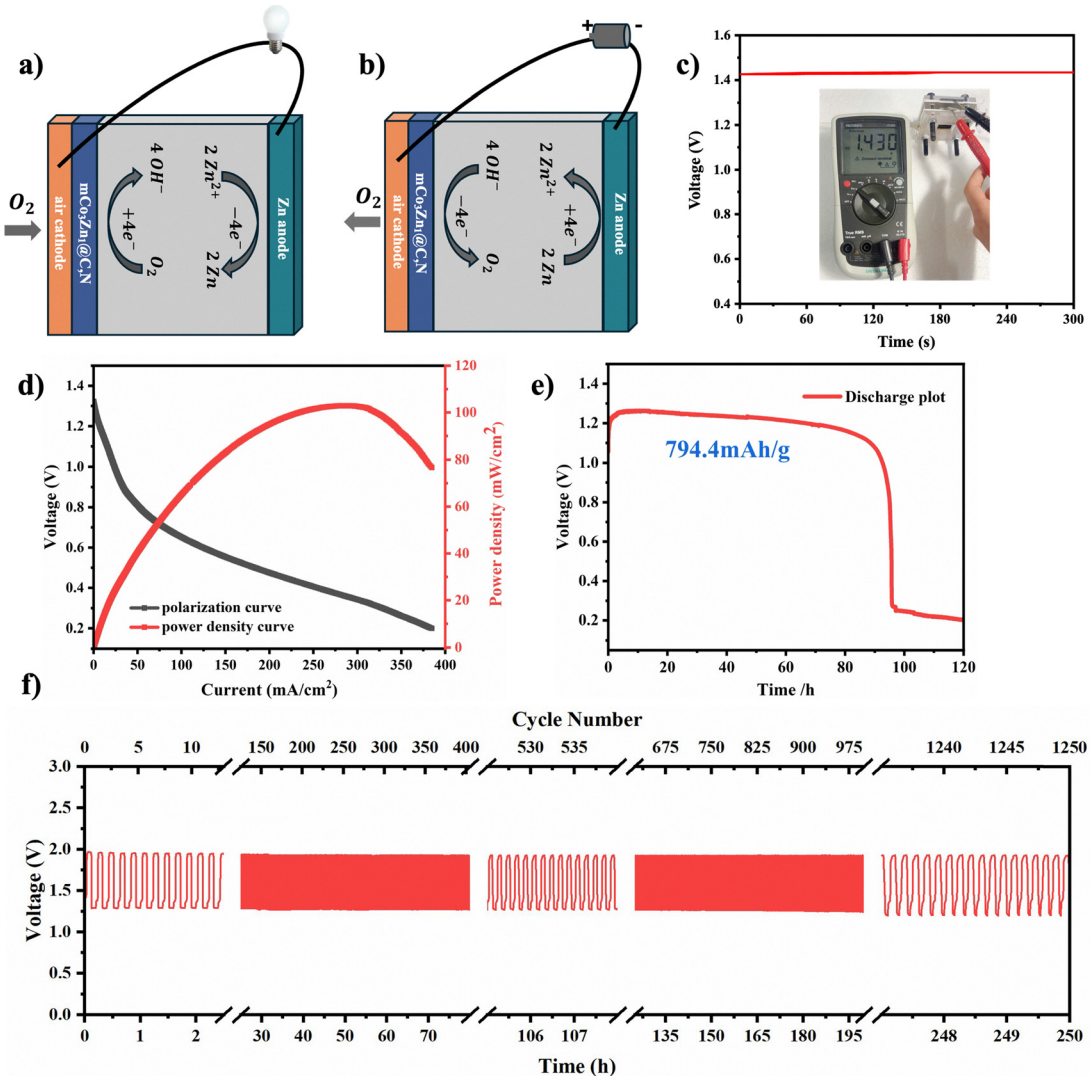

Fig. 7 Illustration of the configuration of a rechargeable ZAB and the internal (a) ORR and (b) OER reaction. (c) Open-circuit voltage plot (red line) and photograph of the ZABs. (d) Polarization and power density curves of the ZABs using mCo_3Zn_1@CN(800) as ORR catalysts. (e) Discharge plot and the corresponding specific capacity of the ZABs normalized by the mass consumption of the Zn plate. (f) Charge/discharge galvanostatic curve of rechargeable ZABs using mCo_3Zn_1@CN(800) as bifunctional air electrode catalysts at a current density of 2 mA cm^{-2}.

capacity reached a maximum value of 794.4 mA h g^{-1}, normalized by the mass consumption of the Zn plate.

The long-term charge–discharge cycling stability was further tested for this zinc–air battery. During this procedure, each cycle lasted for 12 minutes with 6 minutes of charge, and 6 minutes of discharge. As shown in Fig. 7(f), the battery gives remarkable stability for 250 h (1250 cycles) at a current density of 2 mA cm^{-2} particularly compared to a battery made up from benchmark Pt/C and RuO_2 materials (Fig. S17). In the first cycle, the voltage gap is 0.6817 V with a discharge voltage of 1.2883 V and a charge voltage of 1.9700 V, whereas the corresponding trip efficiency is 65.4% where, battery trip efficiency is defined as the ratio of the energy input during charging to the energy that the battery releases during discharge. After the 530th cycle, roughly at the middle of cycle life, the voltage gap is 0.634 V with a discharge voltage of 1.2898 V and a charge voltage of 1.9238 V, whereas the corresponding trip efficiency is 67.0% at its maximum, increased slightly (1.6%) compared to the first cycle. Even after the 1250th cycle, the voltage gap only increased to 0.7227 V with a discharge voltage of 1.1998 V and a charge voltage of 1.9224 V. The trip efficiency drops to 62.4% and merely fades by 3% compared to the first cycle and 4.6% compared to the 530th cycle where maximum trip efficiency was observed.

4. Discussion

The development of bifunctional electrocatalysts for ORR and OER is crucial for advancing zinc–air battery performance. In this study, mCo_xZn_y@CN(T) catalysts derived from Co–Zn bimetallic ZIFs doped with melamine demonstrated remarkable electrocatalytic activity, stability, and efficiency. The incorporation of melamine during synthesis played a significant role in improving catalytic properties by promoting the formation of graphitic carbon and carbon nanotube (CNT) structures, leading to high electronic conductivity, high surface area and well active site distribution.

The XRD, FTIR, and XPS analyses confirm the successful formation of nitrogen-doped graphitic carbon frameworks with embedded cobalt nanoparticles. The presence of Co–N_x active sites, as identified in XPS spectra, is instrumental in enhancing ORR and OER activities. While XPS analysis confirms the presence of Co–N interactions, the exact coordination environment—such as CoN_4 or mixed Co–N_xC_y moieties—cannot be definitively resolved by XPS alone. Therefore, the active sites are referred to here as Co–N_x, consistent with the established terminology in related literature. The N_2 physisorption, SEM and TEM images further reveal a highly porous structure with CNT formation in mCo_3Zn_1@CN(T), which facilitates charge transport and increases the accessibility of catalytic sites. The impact of pyrolysis temperature was evident, with 800 °C found to be optimal for achieving high graphitic carbon content and well-dispersed active sites, enhancing overall electrocatalytic performance. Although Co–N_x sites are well-established ORR active sites, the presence of metallic Co nanoparticles encapsulated within the CNTs may also contributes significantly *via* synergistic effects to the overall catalytic performance. These metal particles can modulate the local electronic structure of Co–N_x sites and facilitate intermediate adsorption and charge transfer, thereby boosting ORR performance. In our system, such confined metallic species are likely to contribute to the observed high activity, in conjunction with the Co–N_x centres—pointing to a dual-site catalytic mechanism supported by previous works in literature.[46]

Electrochemical analysis demonstrated that the mCo_3Zn_1@CN(T) catalyst with Co to Zn ratio of 3, exhibited superior ORR and OER activity compared to non-melamine-doped counterparts and commercial catalysts such as Pt/C and RuO_2. The catalyst exhibited a low OER overpotential of 0.34 V at 10 mA cm^{-2}, a small Tafel slope of 79.95 mV dec^{-1}, and a high onset potential of 0.98 V for ORR. The calculated potential gap (ΔE = 0.68 V) further confirms its excellent bifunctional performance, surpassing many recently reported non-precious metal catalysts. The enhanced activity can be attributed to the synergistic effects of Co–N_x coordination, hierarchical porosity, and the presence of graphitic carbon and CNTs, which optimize charge transfer and reaction kinetics. Additionally, the possible influence of trace amounts of residual Zn—detected in elemental analyses—cannot be excluded, as such species may contribute to structural modulation, porosity development, or even catalytic synergy, particularly in the optimally active mCo_3Zn_1@CN(800) sample. To place our findings in context, a performance comparison between mCo_3Zn_1@CN(800) and other recently reported non-precious bifunctional electrocatalysts is summarised in Table 2. The catalyst demonstrates a competitive half-wave potential for ORR (0.89 V), low required potential for OER at 10 mA cm^{-2} (1.57 V), and a small overall potential gap (ΔE = 0.68 V). These metrics compare favourably to many state-of-the-art

Table 2 Reported OER and ORR electrochemical properties of materials

Catalyst	Electrolyte	$E_{1/2}$ (V)	$E_{j=10,\ OER}$ (V)	η_{OER}	ΔE (V)	Ref.
mCo_3Zn_1@CN(800)	1.0 M KOH	0.89	1.57	0.34	0.68	This study
N-CNT@MOF-Co/HO-BN/CNFs	1.0 M KOH	0.84	1.54	0.31	0.70	47
Co@N-gCarbon	0.1 M KOH	0.76	1.61	0.38	0.85	48
NC@GC	0.1 M KOH	0.93	1.57	0.34	0.64	49
BNPC-1000	0.1 M KOH	0.77	1.69	0.46	0.92	50
$YBaCo_4O_{7.3}$	0.1 M KOH	0.69	1.63	0.40	0.94	51
RuO_2	1.0 M KOH	<0.60	~1.48	~0.25	>0.88	52
Pt/C	1.0 M KOH	~0.86	>1.65	>0.42	>0.79	53

MOF-derived catalysts and metal–nitrogen–carbon (M–N_x–C) systems, highlighting the effectiveness of the synergistic design approach employed in this study.

Long-term cycling tests of the rechargeable Zn–air battery demonstrated exceptional stability, maintaining a high open-circuit voltage of 1.430 V and stable discharge voltages over 250 hours (1250 cycles) at 2 mA cm^{-2}. The minimal voltage decay and stable trip efficiency highlight the robust structural integrity and catalytic durability of mCo_3Zn_1@CN(T). The improved long-term performance is attributed to the strong interaction between Co and N species, preventing active site degradation and ensuring sustained catalytic activity under operational conditions.

The variation in Co/Zn ratios and pyrolysis temperatures revealed significant impacts on catalytic performance. Among the tested compositions, mCo_3Zn_1@CN(800) exhibited the best ORR/OER activity, demonstrating an optimal balance between active site density, electronic conductivity, and structural stability. Higher pyrolysis temperatures (>850 °C) led to the aggregation of Co nanoparticles, reducing active site availability and lowering catalytic efficiency. Conversely, lower pyrolysis temperatures (<700 °C) resulted in incomplete carbonization, yielding lower conductivity and inferior electrochemical performance.

Compared to benchmark Pt/C and RuO_2 catalysts, mCo_3Zn_1@CN(800) offers a cost-effective and sustainable alternative with comparable or superior catalytic performance. The direct integration of recovered metal compounds into the catalyst synthesis process further enhances resource efficiency and sustainability, aligning with circular economy principles. Additionally, the combination of high electrocatalytic activity, excellent cycling stability, and scalable synthesis positions mCo_3Zn_1@CN(800) as a promising candidate for next-generation Zn–air batteries and other energy storage applications.

5. Conclusion

The developed mCo_xZn_y@CN(T) catalyst successfully addresses key challenges in Zn–air battery technology by offering high bifunctional activity and excellent durability. Our results demonstrate that with a metal molar ratio of 3/1 (Co/Zn), with a pyrolysis temperature of 800 °C, and with the presence of melamine, the resultant carbon nanotube including mCo_3Zn_1@CN(800) exhibits superior ORR/OER activities in an alkaline electrolyte, matching commercial benchmark RuO_2 and Pt/C catalysts. The cycling test demonstrated the excellent stability and electrochemical performance of the material as an electrode in zinc air battery with 1250 cycles without obvious performance attenuation. The findings provide valuable insights into the design of efficient and sustainable electrocatalysts for next-generation energy storage systems.

Author contributions

LK: data curation, formal analysis, investigation, methodology, validation, visualization, writing – original draft. VD: conceptualisation, formal analysis, funding acquisition, methodology, project administration, supervision, visualisation, writing – review & editing.

Conflicts of interest

There are no conflicts to declare.

Data availability

Data for this article are available at Warwick Research Archive Portal (WRAP) at **https://wrap.warwick.ac.uk/190443/**.

Supplementary information is available. See DOI: **https://doi.org/10.1039/d5ma00709g**

Acknowledgements

We acknowledge the China Scholarship Council and University of Warwick PhD Scholarship for LK (no. 202204910054). We acknowledge the help and support of David Walker for XRD data collection (Warwick X-ray diffraction RTP), Yining Xie and Yisong Han for STEM-EDX data collection (Warwick microscopy RTP), and Marc Walker (Warwick Photoemission RTP) for XPS data collection and Gwilherm Kerherve for useful insights for analysis.

References

1 Q. Liu, Z. Pan, E. Wang, L. An and G. Sun, *Energy Storage Mater.*, 2020, **27**, 478–505.
2 Q. Wang, S. Kaushik, X. Xiao and Q. Xu, *Chem. Soc. Rev.*, 2023, **52**, 6139–6190.
3 X.-W. Lv, Z. Wang, Z. Lai, Y. Liu, T. Ma, J. Geng and Z.-Y. Yuan, *Small*, 2024, **20**, 2306396.
4 Y.-L. Zhang, K. Goh, L. Zhao, X.-L. Sui, X.-F. Gong, J.-J. Cai, Q.-Y. Zhou, H.-D. Zhang, L. Li, F.-R. Kong, D.-M. Gu and Z.-B. Wang, *Nanoscale*, 2020, **12**, 21534–21559.
5 X. Wu, C. Tang, Y. Cheng, X. Min, S. P. Jiang and S. Wang, *Chem. – Eur. J.*, 2020, **26**, 3906–3929.
6 H. Araújo, B. Šljukić, S. Gago and D. M. F. Santos, *Front. Energy Res.*, 2024, **12**, 1373522.
7 S. Chen, M. Cui, Z. Yin, J. Xiong, L. Mi and Y. Li, *ChemSusChem*, 2021, **14**, 73–93.
8 N. Sun, S. S. A. Shah, Z. Lin, Y.-Z. Zheng, L. Jiao and H.-L. Jiang, *Chem. Rev.*, 2025, **125**, 2703–2792.
9 T. W. Chamberlain, V. Degirmenci and R. I. Walton, *ChemCatChem*, 2022, **14**, e202200135.
10 L. Du, L. Xing, G. Zhang and S. Sun, *Carbon*, 2020, **156**, 77–92.
11 F. Gui, Q. Jin, D. Xiao, X. Xu, Q. Tan, D. Yang, B. Li, P. Ming, C. Zhang, Z. Chen, S. Siahrostami and Q. Xiao, *Small*, 2022, **18**, 2105928.
12 C. H. L. Tempelman, R. Oozeerally and V. Degirmenci, *Catalysts*, 2021, **11**, 861.
13 H. Yang, X. Qian, N. Zhang, X. Jia, Z. Wen and M. Zhou, *New J. Chem.*, 2022, **46**, 13651–13660.

14 X. Duan, S. Ren, N. Pan, M. Zhang and H. Zheng, *J. Mater. Chem. A*, 2020, **8**, 9355–9363.
15 D. Wang, H. Xu, P. Yang, X. Lu, J. Ma, R. Li, L. Xiao, J. Zhang and M. An, *J. Mater. Chem. A*, 2021, **9**, 13678–13687.
16 S. Bhardwaj, T. Boruah and R. S. Dey, *Inorg. Chem. Front.*, 2023, **10**, 7296–7307.
17 S. Gao, K. Lian, X. Wang, X. Liu, A. Abdukayum, Q. Kong and G. Hu, *Small*, 2024, **20**, 2406776.
18 Y. Song, C. Yu, D. Ma and K. Liu, *Coord. Chem. Rev.*, 2024, **499**, 215492.
19 H. Gong, X. Zheng, K. Zeng, B. Yang, X. Liang, L. Li, Y. Tao and R. Yang, *Carbon*, 2021, **174**, 475–483.
20 X. Duan, M. Xia, X. Hu, L. Yang and H. Zheng, *Nanoscale*, 2022, **14**, 16516–16523.
21 Z. Kong, T. Liu, K. Hou and L. Guan, *J. Mater. Chem. A*, 2022, **10**, 2826–2834.
22 Y. Arafat, M. R. Azhar, Y. Zhong, H. R. Abid, M. O. Tadé and Z. Shao, *Adv. Energy Mater.*, 2021, **11**, 2100514.
23 Y. Chu, Q.-L. Jiang, L.-Y. Chang, Y.-H. Jin and R.-Z. Wang, *J. Electroanal. Chem.*, 2023, **928**, 117041.
24 X. Duan, S. Ren, N. Pan, M. Zhang and H. Zheng, *J. Mater. Chem. A*, 2020, **8**, 9355–9363.
25 Z.-Y. Huang, X.-S. Guo, Y. Tang, J.-S. Ye, H.-Y. Liu and X.-Y. Xiao, *J. Alloys Compd.*, 2023, **947**, 169441.
26 K. Sun, X. Lei, X. Xie, W. Li, W. Hou, H. Peng and G. Ma, *J. Energy Storage*, 2024, **98**, 113004.
27 X. R. Wang, J. Y. Liu, Z. W. Liu, W. C. Wang, J. Luo, X. P. Han, X. W. Du, S. Z. Qiao and J. Yang, *Adv. Mater.*, 2018, **30**, 1800005.
28 F. X. Ma, X. Liang, Z. H. Liu, Y. Chen, Z. Q. Liu, W. Zhang, L. Zhen, X. C. Zeng and C. Y. Xu, *Angew. Chem., Int. Ed.*, 2025, e202504935.
29 H. S. Fan, X. Liang, F. X. Ma, G. Zhang, Z. Q. Liu, L. Zhen, X. C. Zeng and C. Y. Xu, *Small*, 2024, **20**, 2307863.
30 H.-S. Fan, F.-X. Ma, Z.-H. Liu, W.-H. Wang, Z.-Q. Liu, X.-Y. Liang, Y. Du, Y.-Y. Li, L. Zhen and C.-Y. Xu, *Rare Met.*, 2024, **43**, 5769–5780.
31 Y. Li, B. Jia, Y. Fan, K. Zhu, G. Li and C. Y. Su, *Adv. Energy Mater.*, 2018, **8**, 1702048.
32 G. Kerherve, KherveFitting, **https://sourceforge.net/projects/khervefitting/files/**, (accessed 04/07/2025, 2025).
33 A. Ahmad, N. Iqbal, T. Noor, A. Hassan, U. A. Khan, A. Wahab, M. A. Raza and S. Ashraf, *J. CO2 Util.*, 2021, **48**, 101523.
34 A. S. Abdelmoaty, A. A. El-Beih and A. A. Hanna, *J. Inorg. Organomet. Polym. Mater.*, 2022, **32**, 1778–1785.
35 R. Wang, L. Jiang, Q. Wang, G.-F. Wei and X. Wang, *Adv. Compos. Hybrid Mater.*, 2023, **6**, 157.
36 H. Jiang, J. Gu, X. Zheng, M. Liu, X. Qiu, L. Wang, W. Li, Z. Chen, X. Ji and J. Li, *Energy Environ. Sci.*, 2019, **12**, 322–333.
37 I. S. Amiinu, X. Liu, Z. Pu, W. Li, Q. Li, J. Zhang, H. Tang, H. Zhang and S. Mu, *Adv. Funct. Mater.*, 2018, **28**, 1704638.
38 Y. Li, B. Jia, Y. Fan, K. Zhu, G. Li and C.-Y. Su, *Adv. Energy Mater.*, 2018, **8**, 1702048.
39 W. Zhou, Y. Li, L. Zheng, J. Liu, R. Tang, K. Shi and Y. Zhang, *CrystEngComm*, 2021, **23**, 4930–4937.
40 D. Saliba, M. Ammar, M. Rammal, M. Al-Ghoul and M. Hmadeh, *J. Am. Chem. Soc.*, 2018, **140**, 1812–1823.
41 S. Aleksandra, L. Balan, V. Falk, L. Aranda, G. Medjahdic and R. Schneider, *CrystEngComm*, 2014, **16**(21), 4493–4500.
42 Y.-L. Wang, P.-Y. Zhao, B.-L. Liang, K. Chen and G.-S. Wang, *Carbon*, 2023, **202**, 66–75.
43 L. Li, P. Dai, X. Gu, Y. Wang, L. Yan and X. Zhao, *J. Mater. Chem. A*, 2017, **5**, 789–795.
44 A. Adhikari, K. Chhetri, R. Rai, D. Acharya, J. Kunwar, R. M. Bhattarai, R. K. Jha, D. Kandel, H. Y. Kim and M. R. Kandel, *Nanomaterials*, 2023, **13**, 2612.
45 W. Li, L. Cheng, X. Chen, Y. Liu, Y. Liu, Q. Liu and Y. Huang, *Nano Energy*, 2023, **106**, 108039.
46 S. Ye, D. Zhang, Z. Ou, L. Zheng, W. Liu, W. Chen, Y. Xu, Y. Li, X. Ren and X. Ouyang, *Adv. Funct. Mater.*, 2024, **34**, 2405884.
47 T. Kim, A. Muthurasu, T. H. Ko, S. H. Chae and H. Y. Kim, *Small*, 2025, 2500033.
48 S. Arthanari, N. Bhuvanendran, V. Dharmaraj, J. E. Park, J. S. Hwang, S. Lee, S. Y. Lee and H. Lee, *ChemSusChem*, 2025, 2500205.
49 Z. Wang, Y. Lu, Y. Yan, T. Y. P. Larissa, X. Zhang, D. Wuu, H. Zhang, Y. Yang and X. Wang, *Nano Energy*, 2016, **30**, 368–378.
50 Y. Qian, Z. Hu, X. Ge, S. Yang, Y. Peng, Z. Kang, Z. Liu, J. Y. Lee and D. Zhao, *Carbon*, 2017, **111**, 641–650.
51 G. P. Kharabe, T. Verma, S. Barik, R. R. Urkude, N. Ayasha, B. Ghosh, S. Krishnamurty and S. Kurungot, *ACS Appl. Mater. Interfaces*, 2025, **17**, 3188–3204.
52 D.-Y. Kuo, H. Paik, J. Kloppenburg, B. Faeth, K. M. Shen, D. G. Schlom, G. Hautier and J. Suntivich, *J. Am. Chem. Soc.*, 2018, **140**, 17597–17605.
53 Z. Zhang, J. Sun, F. Wang and L. Dai, *Angew. Chem., Int. Ed.*, 2018, **130**, 9176–9181.